SUPPLEMENTARY INFORMATION

Low-cost, Resilient, and Non-flammable Rechargeable Fe-ion Batteries with Scalable Fabrication and Long Cycle Life

Yufan Zhang[1+], Chi Ho Lee[2+], Md Zahidul Islam,[3] Joseph Sang-Il Kwon[2*], Choongho Yu[1,3]*

[1] Department of Materials Science and Engineering, Texas A&M University, College Station, Texas, 77843 USA

[2] Department of Chemical Engineering, Texas A&M University, College Station, Texas 77843, United States; Texas A&M Energy Institute, College Station, Texas 77843, United States

[3] Department of Mechanical Engineering, Texas A&M University, College Station, Texas, 77843 USA

[+] Equally contributed to this work.

* Corresponding authors: chyu@tamu.edu (CY), kwonx075@tamu.edu (JSK)

1. FTIR-ATR of CNT and PANI

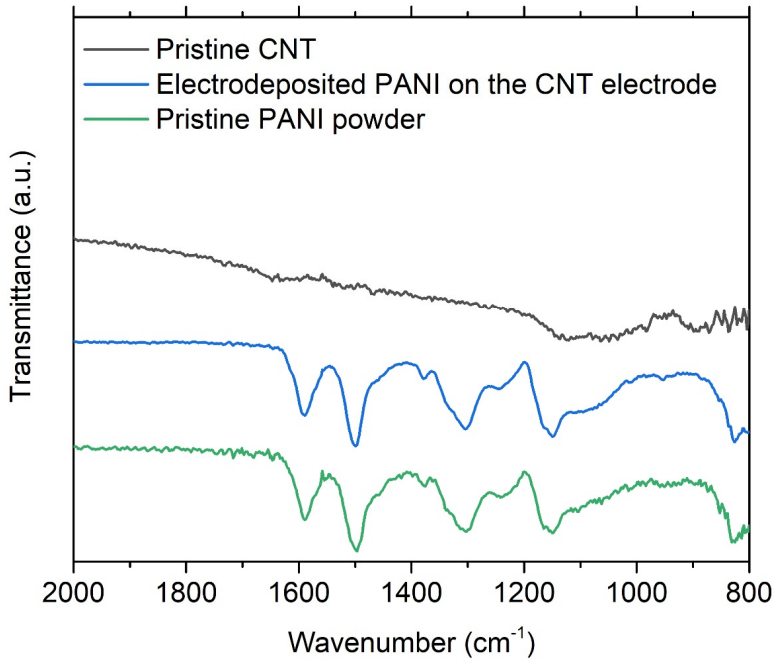

Supplementary Fig. 1. Fourier transform infrared spectroscopy with attenuated total reflectance (ATR-FTIR) of a pristine CNT sponge, electro-deposited PANI on the CNT, and as-purchased PANI powders.

2. Performance of FIB with a composite anode containing iron powders

The carbon steel foil (anode in this work) contains impurities with a limited surface area due to the flat shape of the electrode. Here we have fabricated a composite anode, which is made of 80 wt% iron powders (<10 μm, ≥99.9%; Sigma Aldrich), 10 wt% Super P (particle size: <50 nm; MSE Supplies), and 10 wt% polyvinylidene fluoride (melting point of 155~160 ºC, Beantown Chemical) on a copper substrate. Despite the result showing the plating/stripping efficiency with a copper substrate is the best,[1] the battery performance in **Supplementary Fig. 2** was not superior to that of the carbon steel foil anode.

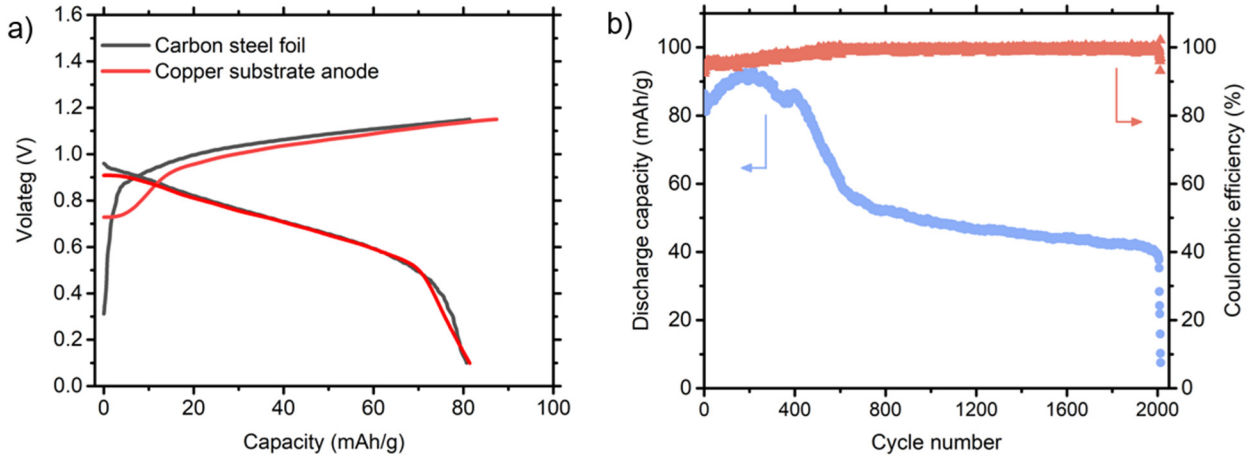

Supplementary Fig. 2. (a) The voltage profiles of Fe-ion batteries with two different anodes – the carbon steel foil and the composite with iron powders when paired with the sandwiched PANI cathode at 5C (cut-off voltage: 1.15V). (b) The cycling performance of the Fe-ion battery with the composite anode at 5 C rate.

3. Cyclic voltammetry (CV)

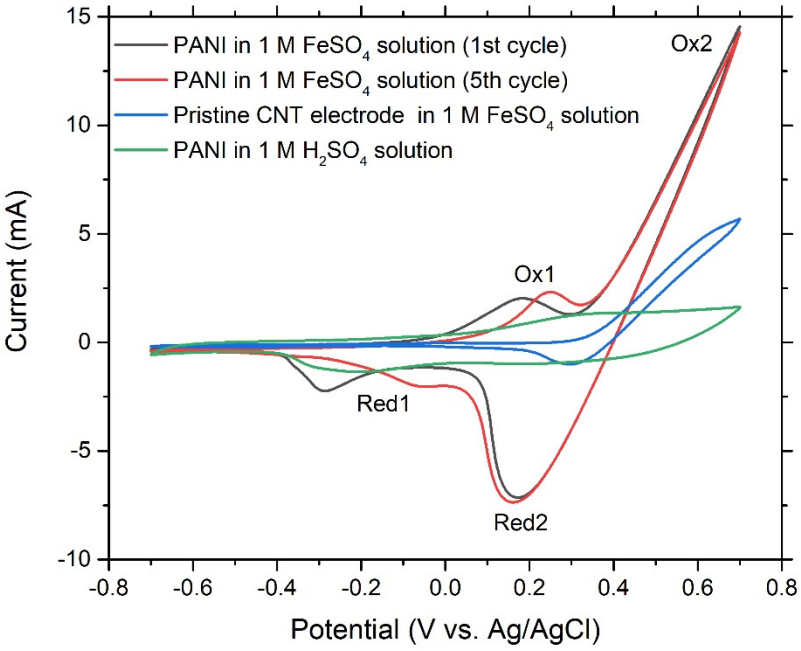

Supplementary Fig. 3. The CV curves of the PANI-embedded CNT and a pristine CNT electrode (working electrode) in two different solutions.

4. The variation of the PANI structure during CV

To determine reasonable intermediate PANI structures with varying Fe concentrations, we utilized Cluster Approach to Statistical Mechanics (CASM), which is a computational method that simplifies the modeling of complex systems by focusing on a representative subset of particles or interactions. This approach is particularly useful in the field of materials science, where the behavior of large assemblies of atoms or molecules is often dictated by localized interactions within smaller clusters. Specifically, in the field of Fe-ion battery systems, the CASM approach requires because it allows us to efficiently screen potential intermediate structures of Fe-incorporated PANI. Also, this method allows for the exploration of different ratios of Fe doping by simulating only the most critical interactions within clusters of atoms. By using this method, it is possible to identify the most promising Fe-PANI structures before proceeding to more extensive and computationally demanding simulations or experimental validations. Specifically, in Fe battery systems, it is crucial to understand the electrochemical properties and phase behaviors across various Fe concentrations. By applying the CASM, we can effectively model clusters representing different phases of the battery materials, with a specific focus on how the Fe ratio impacts the electrochemical performance. We successfully identified stable Fe-incorporated PANI structures, ranging from fully H-incorporated to fully Fe-incorporated. These intermediate PANI structures allowed us to examine the formation energies across varying Fe concentrations during the reductive process. This analysis is pivotal for understanding the significant peak shifts observed during the initial CV cycles. Furthermore, identifying these intermediate PANI structures is essential for elucidating the reasons behind the observed electrochemical performance during oxidative and reductive processes, demonstrating the effectiveness of CASM in providing deep insights into the electrochemical behavior of PANI structures.

5. Preliminary investigation of theoretical method

To efficiently reduce the computational time and system complexity, we have preliminarily investigated two theoretical factors considered in the VASP method: energy convergence and solvation effect. First, regarding the energy convergence factor, we have conducted test calculations with two different theoretical options of 0.04 and 0.01 eV/Å. Specifically, we investigated structural deformation of PANI structures with different Fe ratios during initial stage of the CV cycles, and activation energies of Fe^{2+} cation transfer from SO_4^{2-} anion to nitrogen site. The calculated results in Supplementary Tables 1 and 2 revealed that there is no significant difference between 0.04 and 0.01 eV/Å convergence criteria. Based on these findings, one can envision that 0.04 eV/Å convergence criteria are enough to describe the electrochemical behavior by effectively reducing computational cost. Second, regarding the solvation effect, we conducted test calculations by recognizing the potential importance of solvation effects in the electrochemical behavior of PANI systems. Specifically, to assess the significance of solvation effects, we examined the formation energies of intermediate PANI structures incorporating different Fe concentrations within an implicit water solvent environment. This approach was crucial for verifying the integrity of the intermediate structures and understanding their role in the electrochemical behavior of Fe-ion battery systems, particularly regarding changes in geometric and electronic properties, Fe diffusion barriers, and voltage values. For these calculations, we employed the VASP and VASPsol method to simulate conditions with and without an implicit water solvent, respectively. As listed in the Supplementary Table 3, our findings show negligible differences in formation energies and consistent trends, regardless of the presence of solvent. Based on this evidence, we did not consider the solvation effects in this study to reduce the computational time.

Supplementary Table 1. Structural deformations of stable PANI structures with different Fe concentrations during initial stage of the CV cycles.

PANI structures	0.04 eV/Å	0.01 eV/Å
Fe0.0	26.79°	25.15°
Fe0.25	26.86°	26.19°
Fe0.625	31.06°	31.52°
Fe0.75	34.59°	34.97°
Fe1.0	34.39°	34.41°

Supplementary Table 2. Activation energy barriers for the Fe^{2+} cation transfer from SO_4^{2-} anion to nitrogen site based on consecutive mechanism.

Fe diffusion barrier	0.04 eV/ Å	0.01 eV/ Å
0.125 → 0.25	0.36 eV	0.32 eV
0.5 → 0.625	0.41 eV	0.39 eV
0.625 → 0.75	0.58 eV	0.54 eV
0.875 → 1.0	0.70 eV	0.73 eV

Supplementary Table 3. Formation energies of intermediate PANI structures with different Fe concentrations.

Formation E (eV)	VASP	VASPsol
Fe0.25	-0.15	-0.19
Fe0.375	-0.17	-0.20
Fe0.625	-0.21	-0.27
Fe0.875	-0.10	-0.14

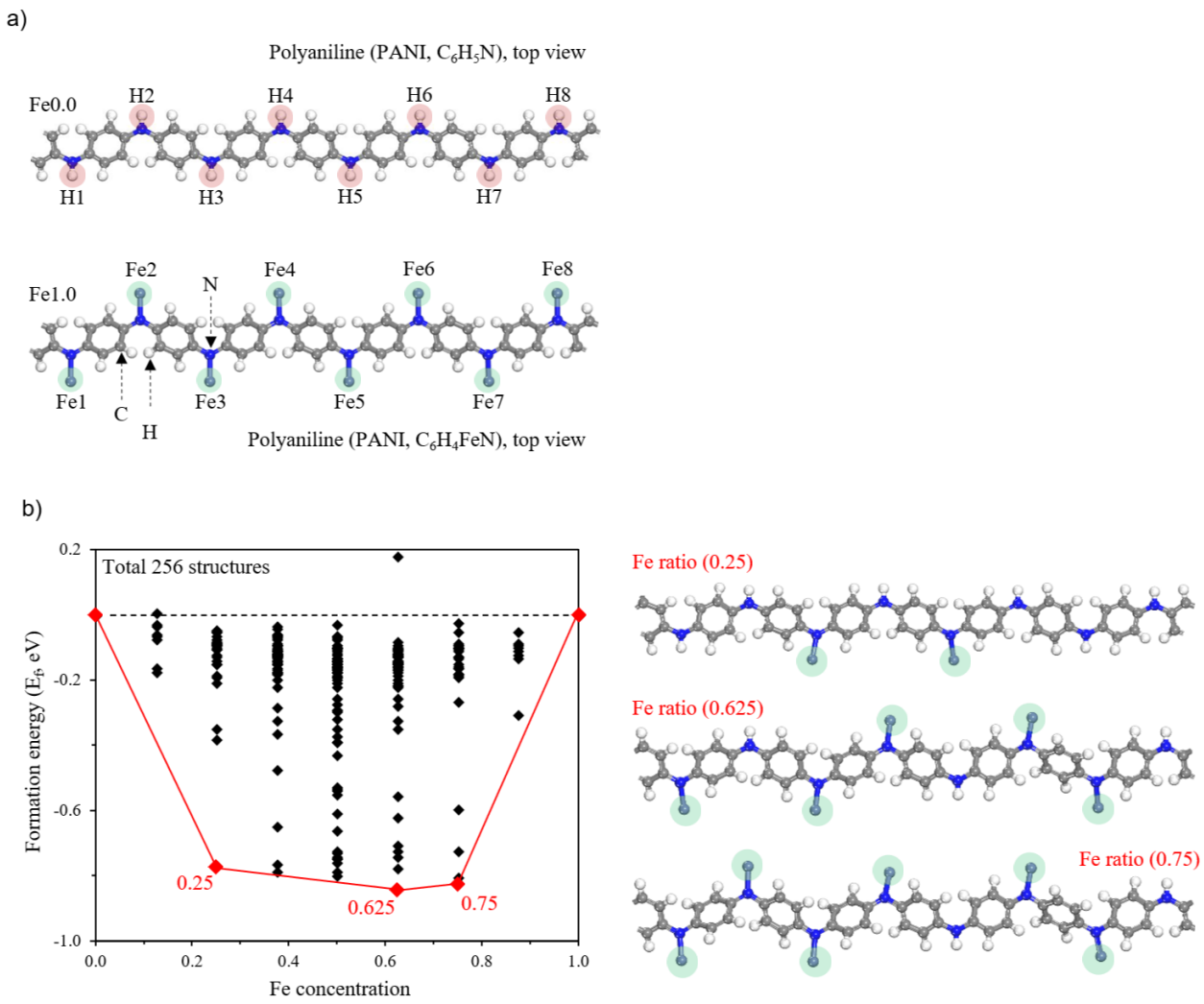

Supplementary Fig. 4. (a) PANI structure with hydrogen (C_6H_5N) and Fe (C_6H_4FeN) that can be generated during the CV cycles. (b) The convex hull diagram of formation energy with Fe attachment in PANI structure during the initial stage of CV. All considered phases are shown as black circles, and stable phases (Fe ratios are 0.25, 0.625, and 0.75 with corresponding formation energies of -0.77 eV, -0.94 eV, and -0.82 eV, respectively) are highlighted with filled red symbols.

To determine appropriate initial structures for Fe^{2+} transfer under two distinct mechanisms, we relied on stable intermediate structures identified through the convex hull analysis. As shown in the left panel of **Supplementary Fig. 6**, for the consecutive mechanism, which involves sequential Fe attachment, we selected initial structures ($Fe_{0.125}$, $Fe_{0.5}$, $Fe_{0.625}$, and $Fe_{0.875}$). These were aligned with corresponding final structures ($Fe_{0.25}$, $Fe_{0.625}$, $Fe_{0.75}$, and $Fe_{1.0}$) to compute activation energies. In contrast, the concerted mechanism, which is characterized by simultaneous Fe attachment, required different initial structures ($Fe_{0.0}$, $Fe_{0.25}$, $Fe_{0.25}$, and $Fe_{0.75}$), aligned with the same final structures, to facilitate the calculation of activation energies. This approach integrates the understanding of stable intermediates ($Fe_{0.25}$, $Fe_{0.625}$, and $Fe_{0.75}$), along with $Fe_{0.0}$ and $Fe_{1.0}$ to predict the most feasible pathways for Fe^{2+} transfer in each mechanism. The right panel presents schematics of varying initial structures, depending on the type of mechanism. In line with the aforementioned explanation, to achieve the $Fe_{1.0}$ PANI structure, the $Fe_{0.75}$ PANI structure is applicable for the concerted mechanism. Conversely, the $Fe_{0.875}$ PANI structure is selected for the consecutive mechanism, demonstrating the mechanism-specific approach to develop the desired $Fe_{1.0}$ PANI configuration.

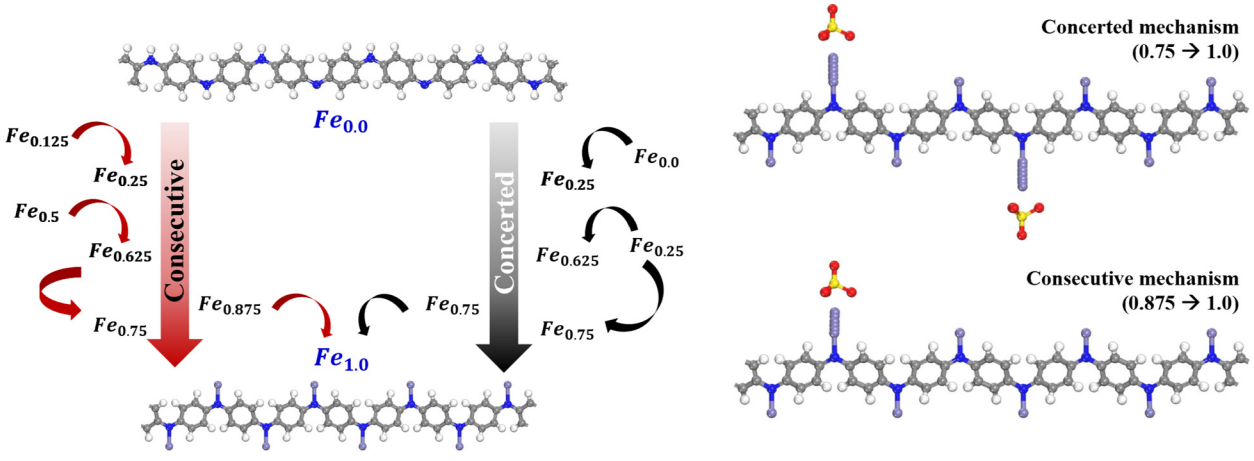

Supplementary Fig. 5. Plausible mechanisms for the Fe^{2+} cation transfer from SO_4^{2-} anion to emptied nitrogen site.

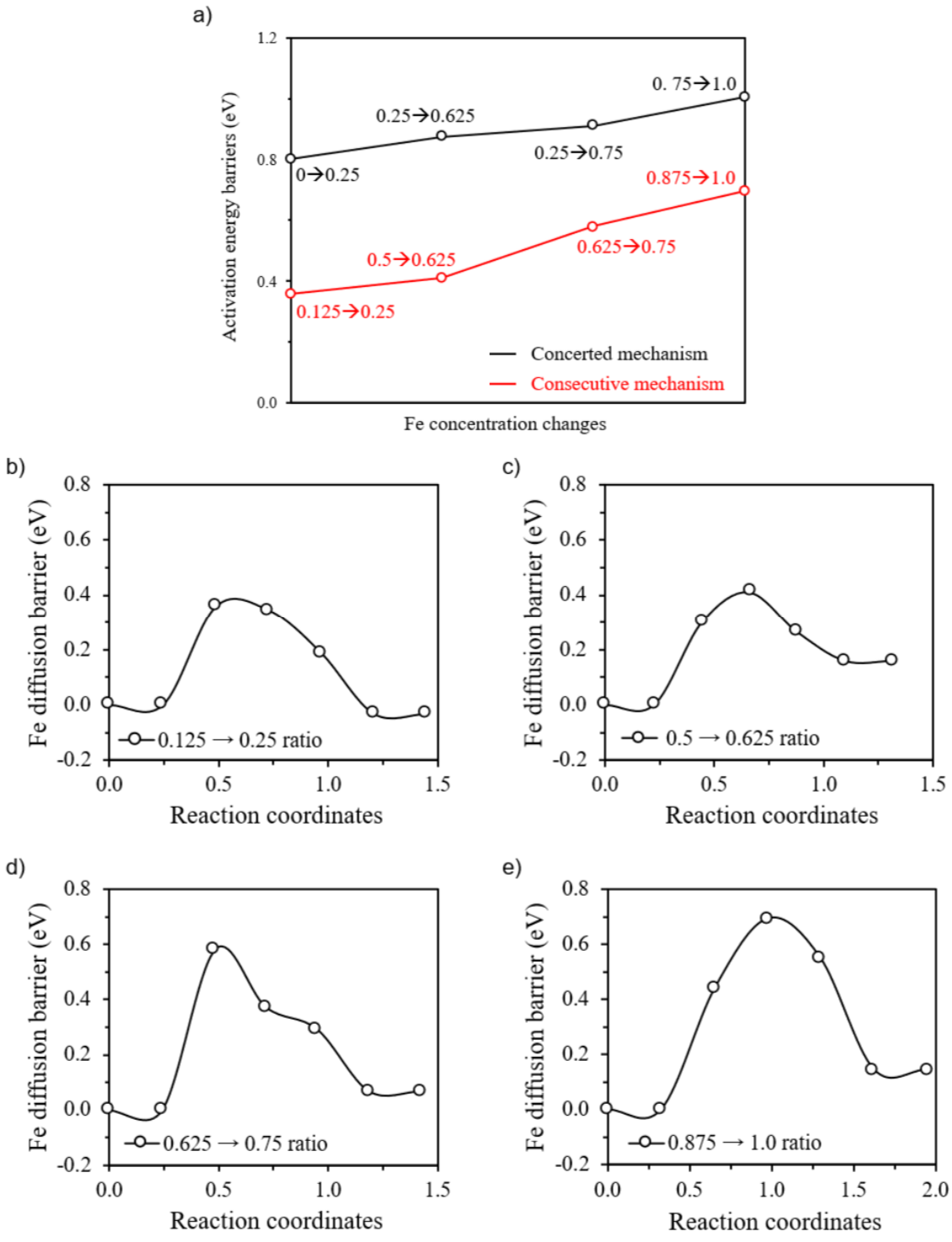

Supplementary Fig. 6. (a) Activation energy barriers for the Fe^{2+} cation transfer from SO_4^{2-} anion to nitrogen site based on the consecutive and concerted mechanisms. (b)-(e) Detailed nudged elastic band (NEB) profile based on the consecutive mechanism that is favorable in the discharging process.

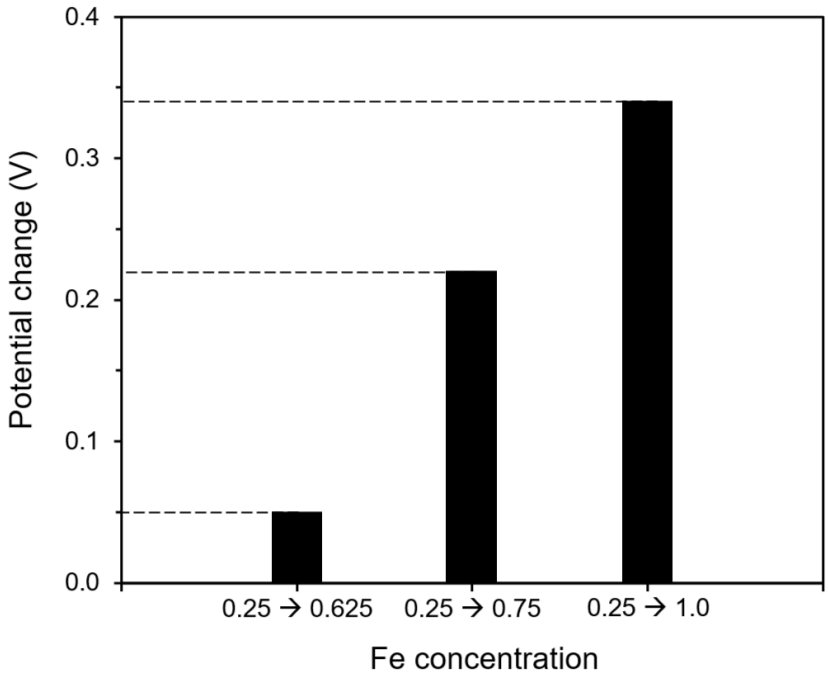

Supplementary Fig. 7. Three distinct theoretical potential variations derived from the Fe0.25 baseline.

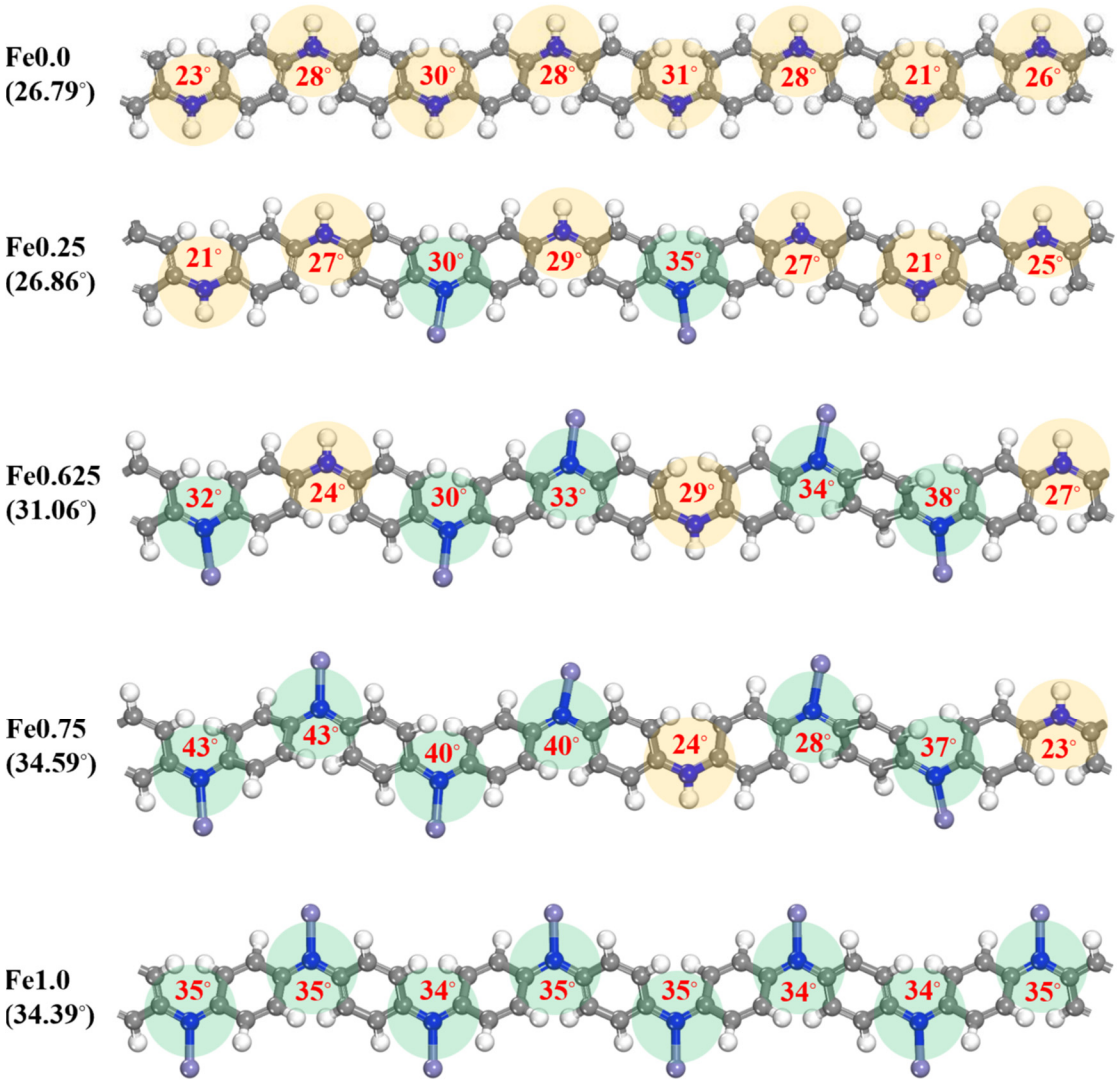

Supplementary Fig. 8. Structural deformations of stable PANI structures with different Fe concentrations during the initial stage of the CV cycles.

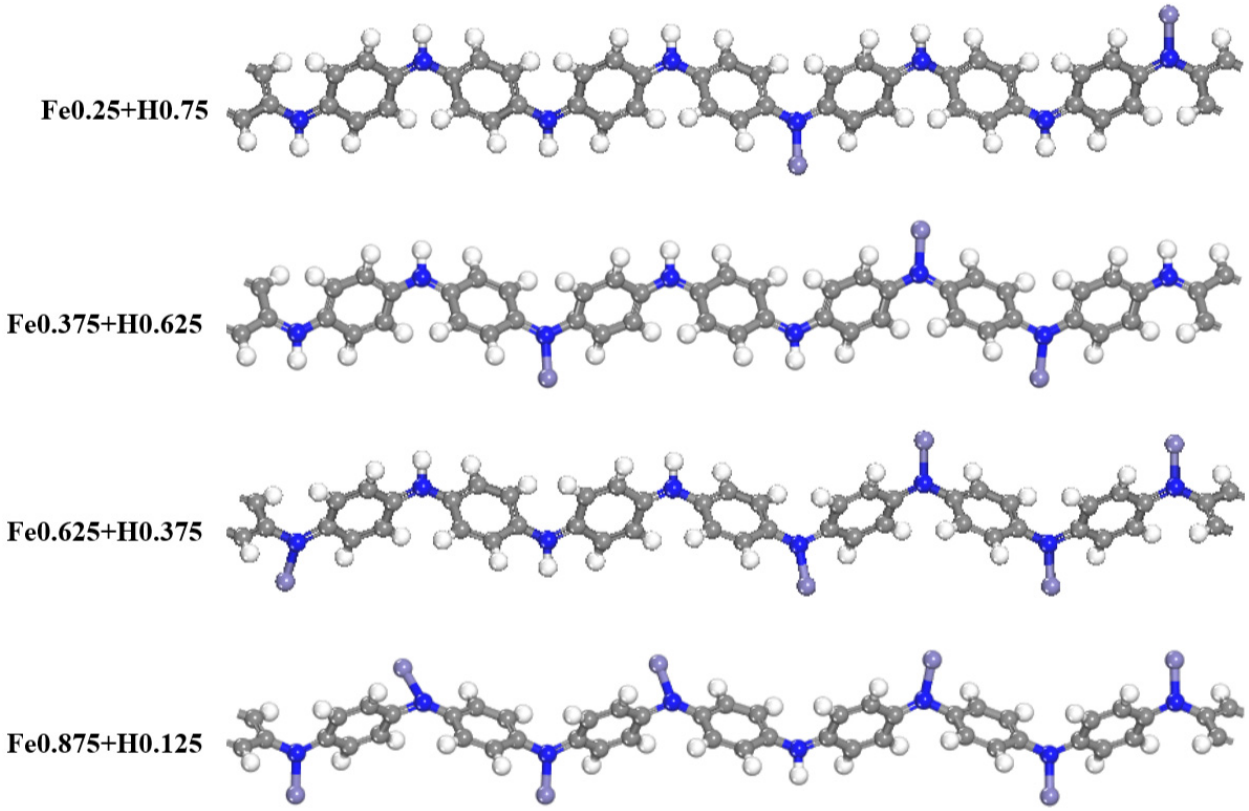

Supplementary Fig. 9. Four different (Fe+H)-attached PANI structures.

6. Structural deformation induced by discharging process with extended time

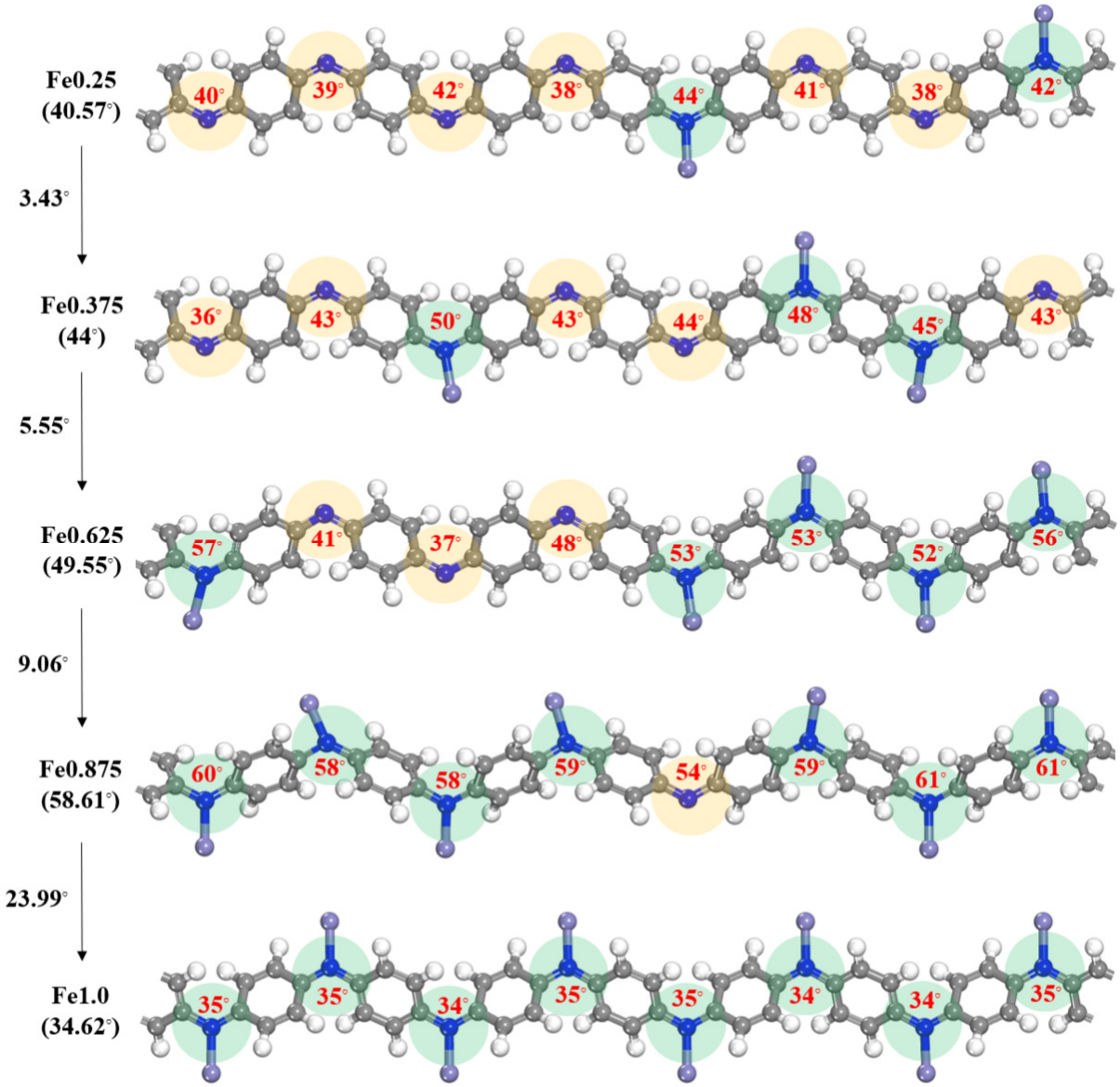

Supplementary Fig. 10. Structural deformations of stable PANI structures with different Fe concentration that can be generated during the discharge process with the extended time.

7. Ex-situ XPS on cathode

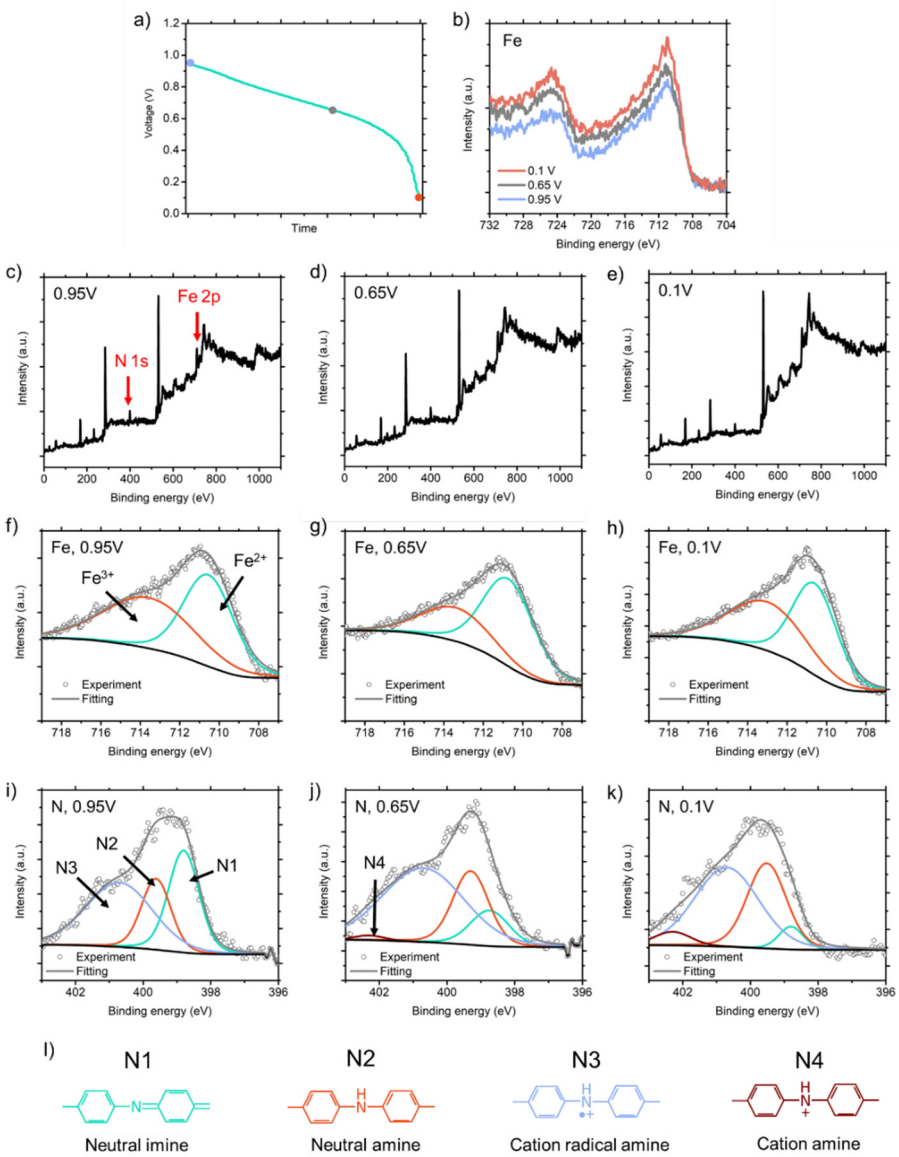

Supplementary Fig. 11. (a) Discharge voltage profile of our Fe-ion battery. (b) Ex-situ XPS spectra of Fe 2p for the cathode at different discharge states, normalized by N 1s intensities. (c), (d), and (e) Ex-situ XPS spectra of the cathodes at 0.95 V, 0.65 V, and 0.1V, respectively. (f), (g), and (h) Resolved XPS spectra of Fe 2p for the cathode at 0.95 V, 0.65 V, and 0.1V, respectively. The resolved Fe 2p spectra indicate the presence of both Fe^{2+} and Fe^{3+}.[2] The detection of Fe^{3+}, however, may result from the oxidation of Fe^{2+} during the washing and drying processes. (i), (j), and (k) Resolved XPS spectra analysis of N 1s for the cathode at 0.95 V, 0.65 V, and 0.1V, respectively. (l) Different nitrogen bonding environments in PANI.

Supplementary Table 4. Atomic %'s of Fe normalized by those of N for the cathodes and their ratios at the three different discharge states from ex-situ XPS analyses.

Voltage	Fe at.% / N at.%	Fe at.% : N at.%
0.95 V	0.365	26.74 : 73.26
0.65 V	0.436	30.37 : 69.63
0.1 V	0.581	36.77 : 63.23

8. Charge and discharge performance for different loading of PANI

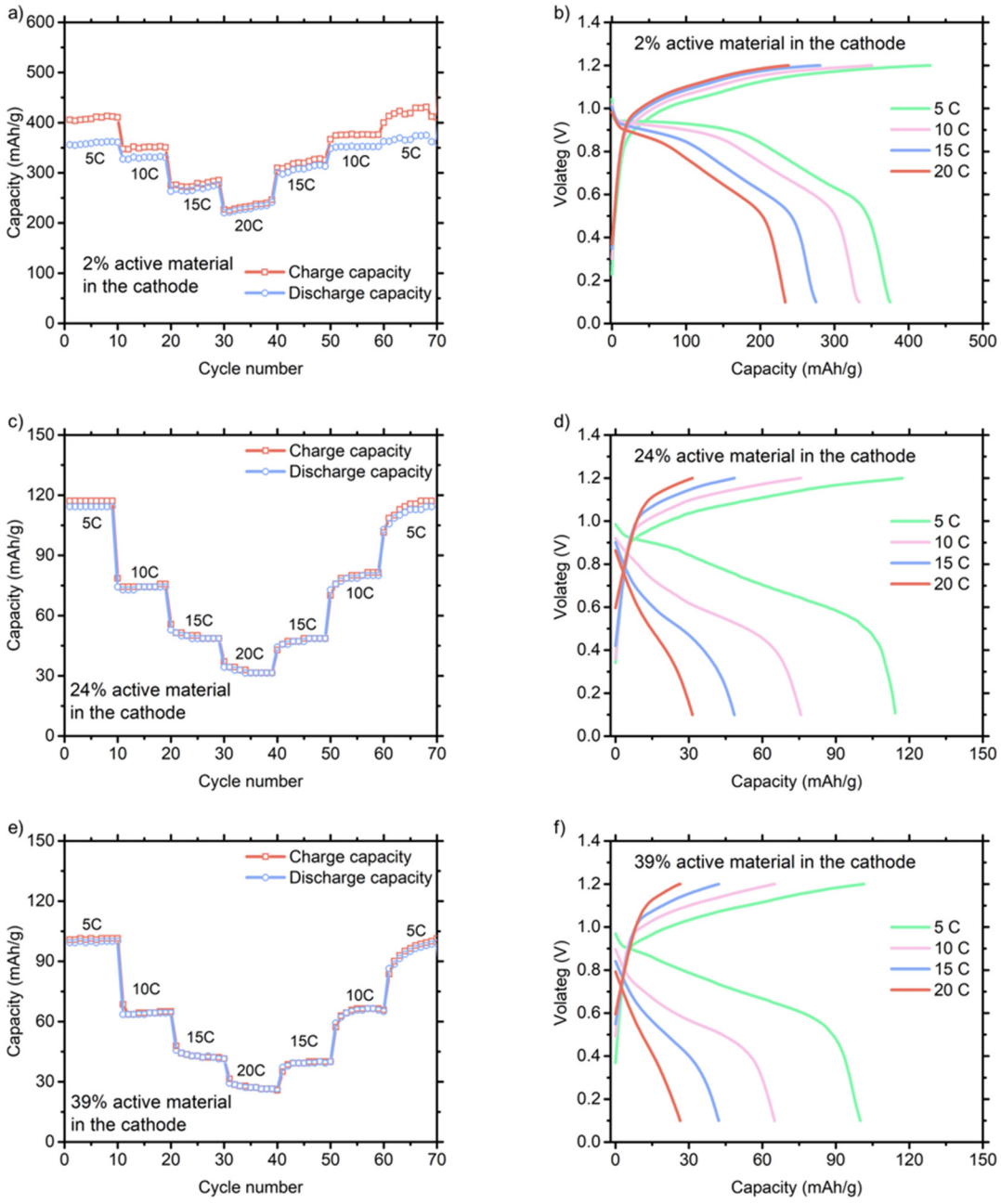

Supplementary Fig. 12. (a) Specific capacity and (b) Charge/discharge curves of the full cell with the 2% active material loading in the PANI-sandwiched CNT cathode at different C rates (1 C = 300 mA per gram). Specific capacities and Charge/discharge curves for (c, d) 24 wt.% and (e, f) 39 wt.% active material loadings.

9. Voltage profiles of pristine CNT in a full cell configuration

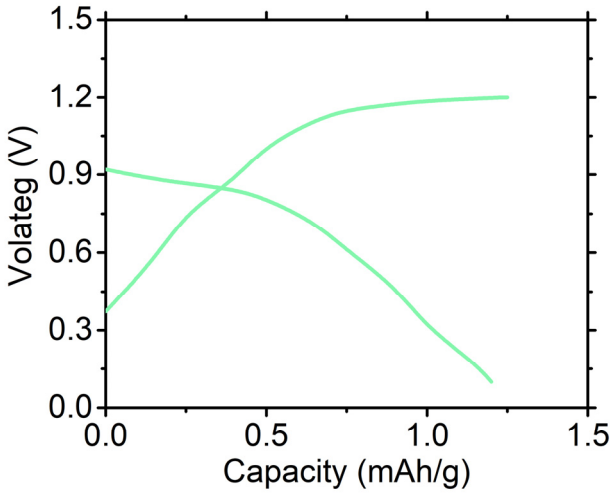

Supplementary Fig. 13. Charge/discharge voltage profiles of a Fe-ion cell with a CNT-only cathode without PANI (CNT loading of 3 mg/cm^2) at a current density of 0.5 mA/g.

10. Voltage profiles for low C rates

The rate capability tests at 0.5~10 C rates for the cells with a loading of 39 wt.% active material were carried out, as displayed in **Supplementary Fig. 14a** and corresponding charge/discharge voltage profiles are shown in **Supplementary Fig. 14b**. As the oxidation of Fe^{2+} may limit the voltage of Fe-ion batteries, our Fe-ion batteries with the PANI-sandwiched CNT cathode were charged up to 200 mAh/g at five different C rates. Their voltage profiles are displayed in **Supplementary Fig. 14c**. When raising the C rate, the saturation voltage during the charge gets higher, which is indicated as short lines in **Supplementary Fig. 14d**. When the charge voltage is above the potential at the saturation in the experiment, the oxidation of Fe^{2+} occurs, lowering the Coulombic efficiency. Therefore, our cells for the performance tests were cycled by limiting the voltage in order not to overshoot the voltage beyond the saturation potential.

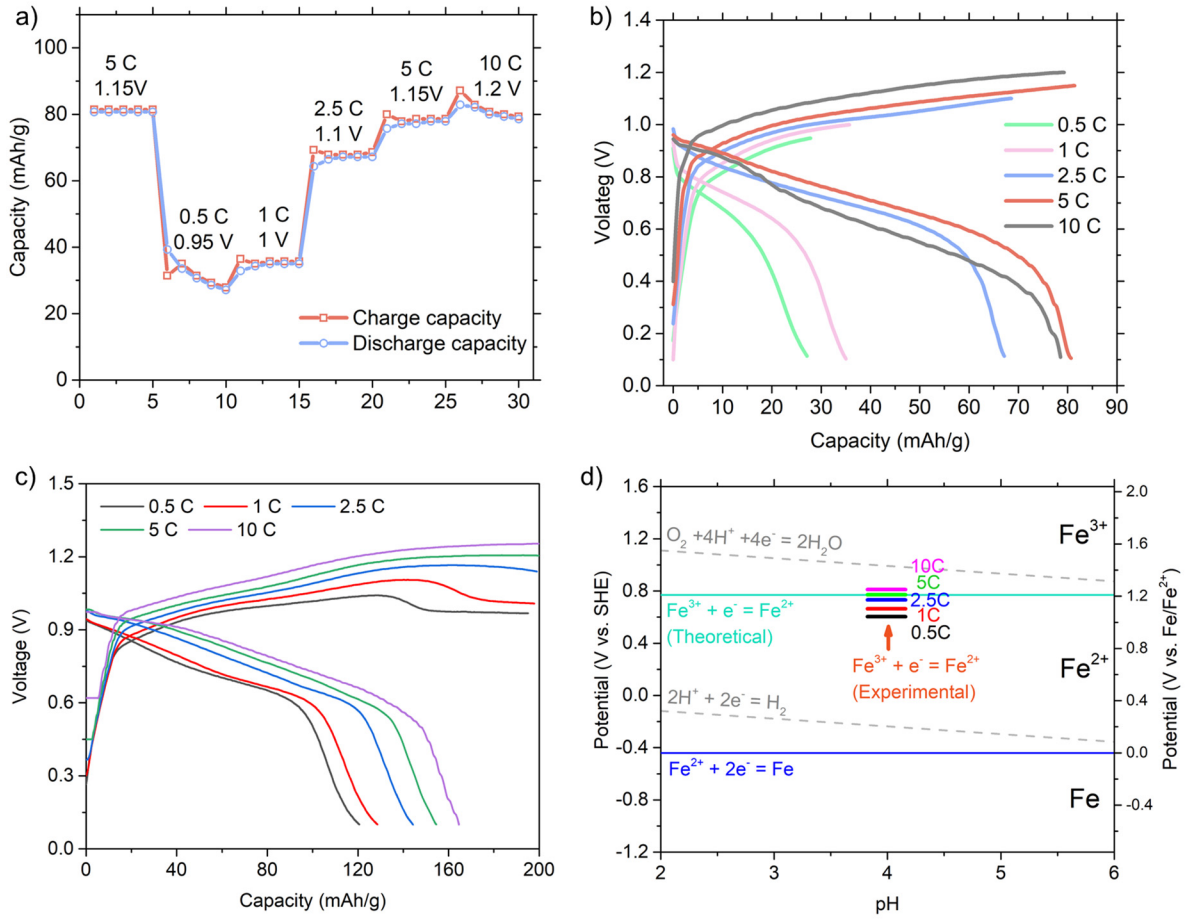

Supplementary Fig. 14. (a) Specific capacity of the full cell with 39% PANI loading in cathode at different C rates (1 C = 300 mA per gram) and corresponding cut-off voltages. (b) Charge/discharge voltage profiles at the different C rates. (c) The voltage profiles of our FIB with the PANI-sandwiched CNT cathode at five different C rates when charging up to a specific capacity of 200 mAh per gram of PANI. (d) Pourbaix diagram with theoretical iron and Fe^{2+}/Fe^{3+} redox potentials (pH is ~4 in aqueous 1M $FeSO_4$ electrolyte). The short lines with 0.5C, 1C, 2.5C, 5C, and 10C indicate the saturation voltages during charge.

11. Cycling performance for different cells

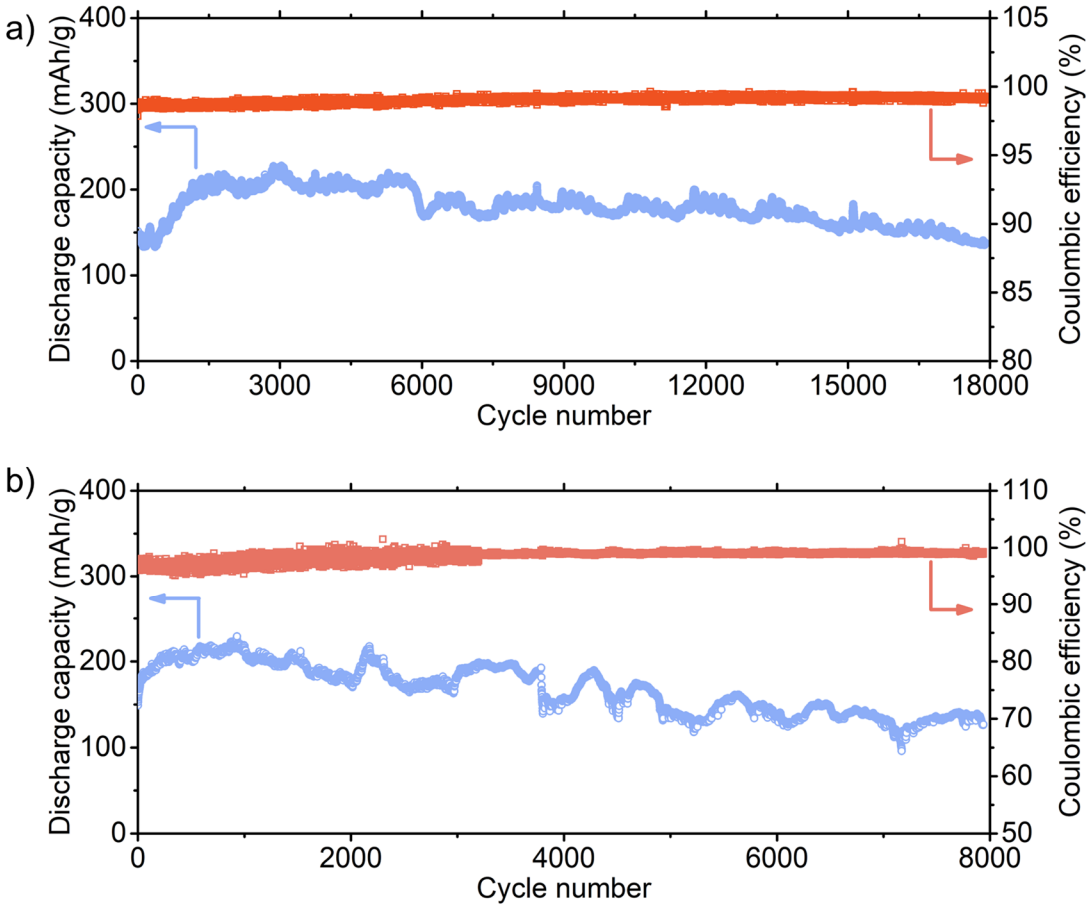

Supplementary Fig. 15. (a) and (b) Specific discharge capacity and Coulombic efficiency for different repetitive cells as a function of cycle number at 15 C for 8 wt.% active material loading cell with 1.2 V cut-off voltage.

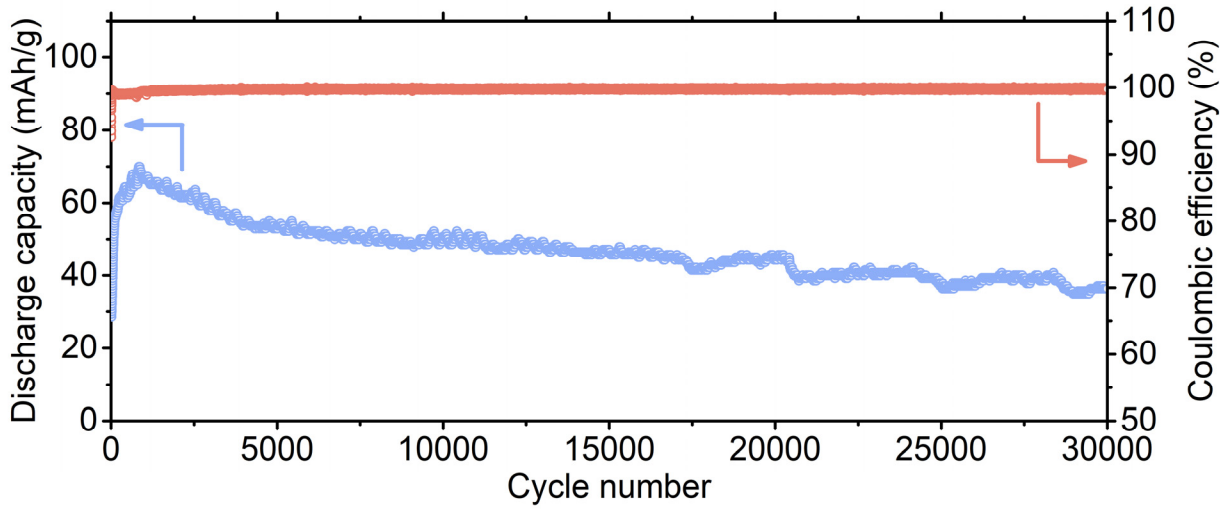

Supplementary Fig. 16. Specific discharge capacity and Coulombic efficiency as a function of cycle number at 5 C for 39 wt.% active material loading cell with 1.15 V cut-off voltage.

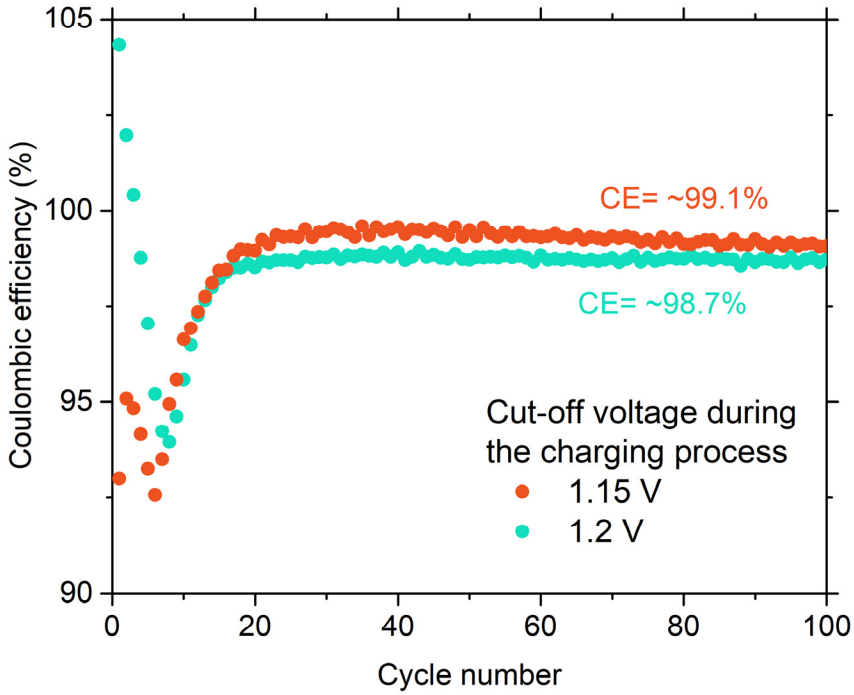

Supplementary Fig. 17. Coulombic efficiency vs. cycle number of the full cell with 39 wt.% active material loading in the cathode for different cut-off voltages during the charging process at 5C.

The Coulombic efficiency for the first 100 cycles at different cut-off voltages during the charging process is shown in **Supplementary Fig. 17**. As the charging voltage increased from 1.15 V to 1.2 V, the Coulombic efficiency of stable charging/discharging cycles decreased from ~99.1% to ~98.7%. This reduction in efficiency indicates that side reactions became more prevalent at the higher voltage.

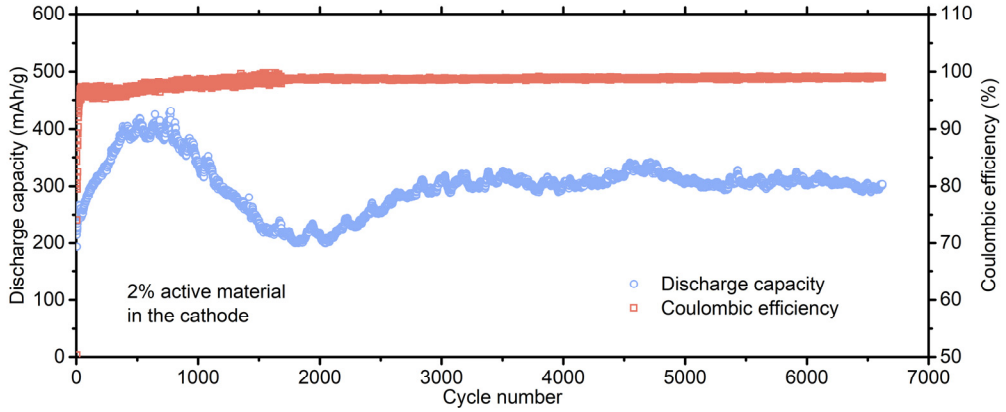

Supplementary Fig. 18. Specific discharge capacity and Coulombic efficiency as a function of cycle number at 15 C for 2 wt.% active material loading of the PANI-sandwiched CNT cathode with 1.2V cut-off voltage.

12. Sandwich-type cathode after cycling

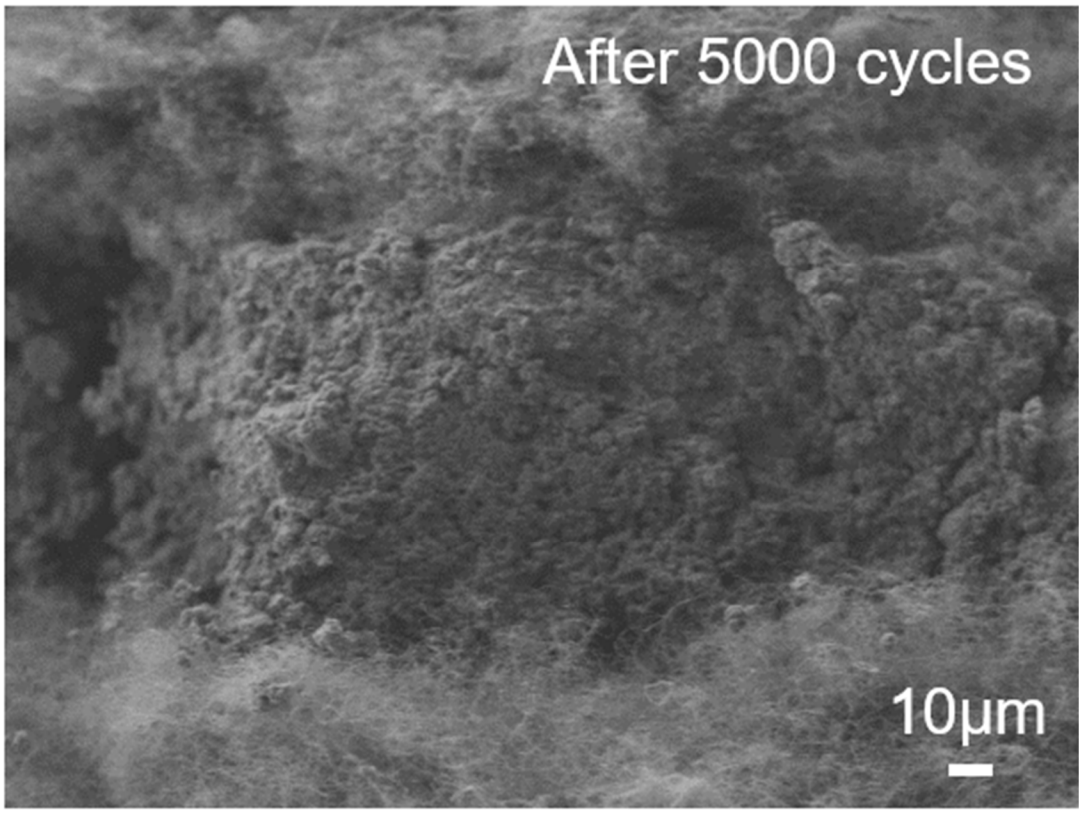

Supplementary Fig. 19. The SEM image of the sandwich-type cathode after 5,000 cycles.

13. XPS spectra of carbon steel anode after cycling

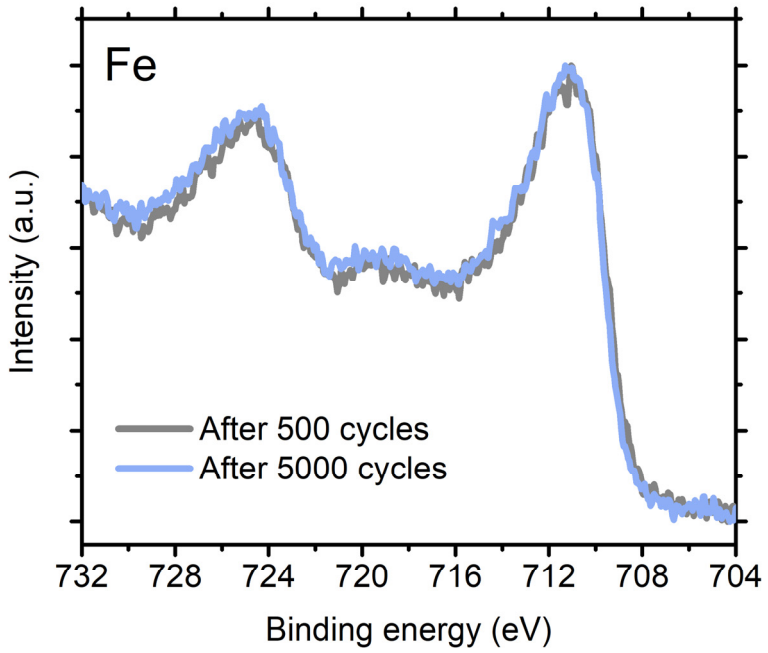

Supplementary Fig. 20. XPS spectra of Fe 2p for carbon steel anode after 500 cycles and 5000 cycles.

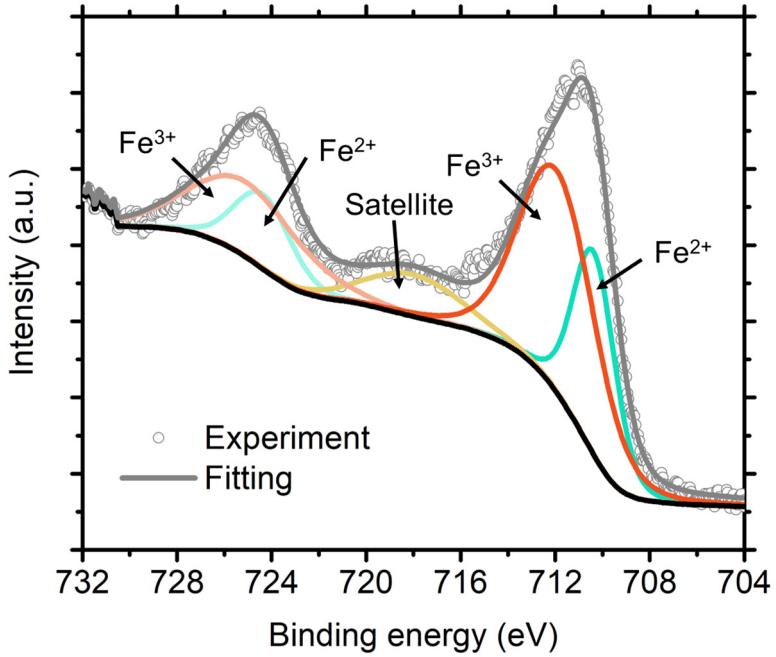

Supplementary Fig. 21. XPS spectra analysis of Fe 2p for carbon steel anode after 500 cycles.

14. Carbon steel anode after cycling

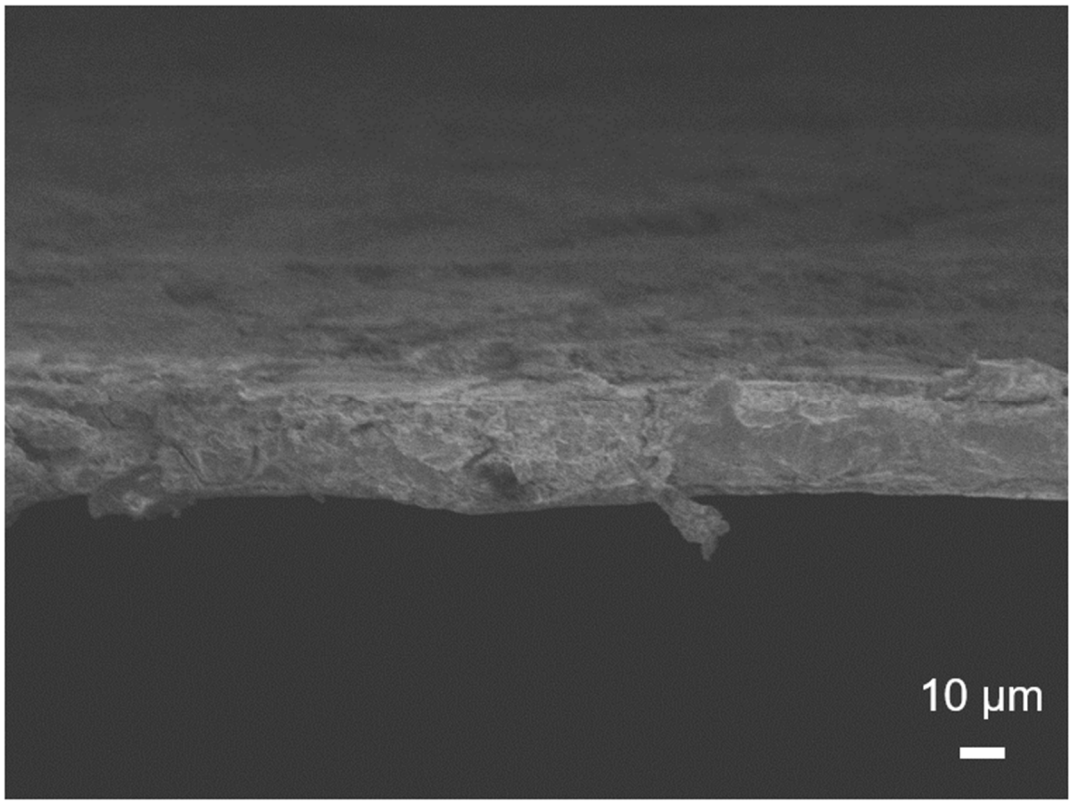

Supplementary Fig. 22. The SEM image of the cross section of a carbon steel anode after 5,000 cycles.

15. External short-circuit test

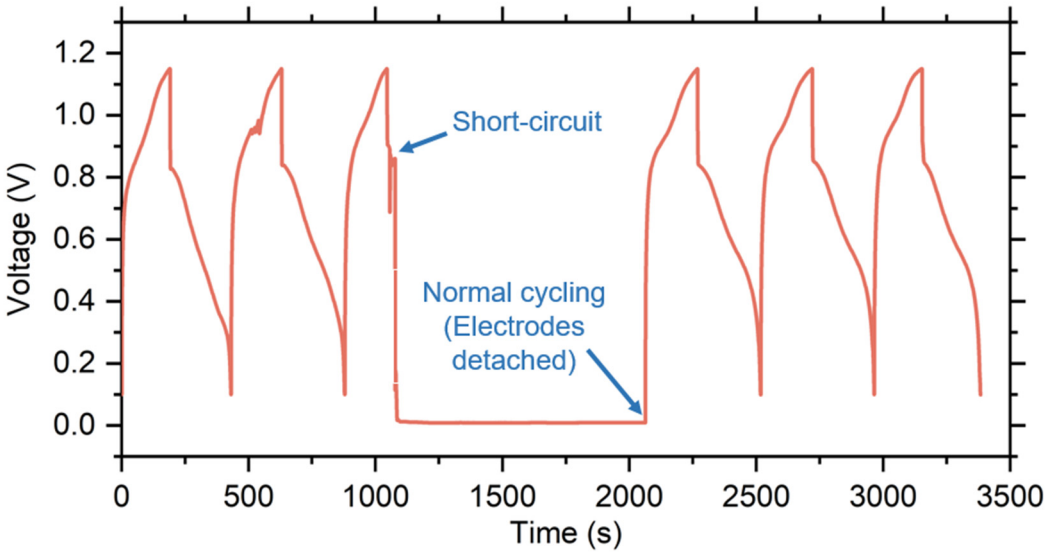

Supplementary Fig. 23. The voltage profile against time for the external short-circuit test.

16. Comparison of this work with lead-acid and Li-ion batteries

Supplementary Table 5. Key performances of this work (Fe-ion batteries), lead-acid and Li-ion batteries.

	This work	Lead-acid batteries	Li-ion batteries
Cycles	30,000	500~1,500 Ref.3	300~2,000 Ref.4
Material cost per kWh ($/kWh)	30-35	100 Ref.5	40-60 Ref.6
Cost efficiency ($/kWh/cycle)	1×10^{-3}	6.67×10^{-2}	2×10^{-2}
Energy density (Wh/kg)	35 *	35~50 Ref.3	150~250 Ref.7
Power density (W/kg)	1,000	150 Ref.8	500 Ref.9
Non-toxicity	Excellent	Poor	Moderate
Safety	Excellent	Moderate	Poor

* Assume that N:P ratio is 2:1. The masses of electrolyte and separator are assumed to be negligible.

Supplementary Table 6. The estimated material cost of our Fe-ion batteries.

Component	Price ($/kg)	Amount of materials used (kg/ kWh)	Price ($/kWh)
Carbon steel [a]	0.06	3.0	0.18
PANI	2.08 Ref.10, [b]	8.5	17.68
Carbon material synthesized in the lab	1 [c]	8.5	8.5
$FeSO_4$ $7H_2O$	0.03	178	5.34
Cellulose filter paper			0.5
Total			**32.2**

[a] N:P ratio is assumed to be 2:1.

[b] The price of PANI is expected to be lower than this value, if mass-produced. The exchange rate between US dollar and CNY is 1:7.21 in Nov. 2023

[c] Use the price of acetylene black for this calculation.

References

1 Wu, X. *et al.* A rechargeable battery with an iron metal anode. *Adv Funct Mater* **29**, 1900911 (2019).

2 Chen, Z.-Y. *et al.* Investigation of Fe2N@carbon encapsulated in N-doped graphene-like carbon as a catalyst in sustainable zinc–air batteries. *Catalysis Science & Technology* **7**, 5670-5676 (2017).

3 Chen, H., Xu, Y., Liu, C., He, F. & Hu, S. in *Storing Energy (Second Edition)* (ed Trevor M. Letcher) 771-791 (Elsevier, 2022).

4 Preger, Y. *et al.* Degradation of commercial lithium-ion cells as a function of chemistry and cycling conditions. *J Electrochem Soc* **167**, 120532 (2020).

5 Mongird, K. *et al.* 2020 grid energy storage technology cost and performance assessment. *Energy* **2020** (2020).

6 Greenwood, M., Wentker, M. & Leker, J. A bottom-up performance and cost assessment of lithium-ion battery pouch cells utilizing nickel-rich cathode active materials and silicon-graphite composite anodes. *Journal of Power Sources Advances* **9**, 100055 (2021).

7 Galos, J. *et al.* Energy Storage Structural Composites with Integrated Lithium-Ion Batteries: A Review. *Advanced Materials Technologies* **6**, 2001059 (2021).

8 Aktaş, A. & Kirçiçek, Y. in *Solar Hybrid Systems* (eds Ahmet Aktaş & Yağmur Kirçiçek) 87-125 (Academic Press, 2021).

9 Zuo, W. *et al.* Battery-Supercapacitor Hybrid Devices: Recent Progress and Future Prospects. *Advanced Science* **4**, 1600539 (2017).

10 Li, Y., Wang, H., Yn, T., Li, J. & Kan, J. Cheap and eco-friendly synthesis of polyaniline and performance of aqueous Zn-polyaniline battery. *Int J Electrochem Sci* **15**, 5956-5965 (2020).